Irregular wave propagation with a 2DH Boussinesq-type model and an unstructured finite volume scheme

M Kazolea, A I Delis

Irregular wave propagation with a 2DH Boussinesq-type model and an unstructured finite volume scheme

M. Kazolea, A.I. Delis

RESEARCH REPORT
N° 9008
December 2016
Project-Teams Cardamom

ISSN 0249-6399 ISRN INRIA/RR--9008--FR+ENG

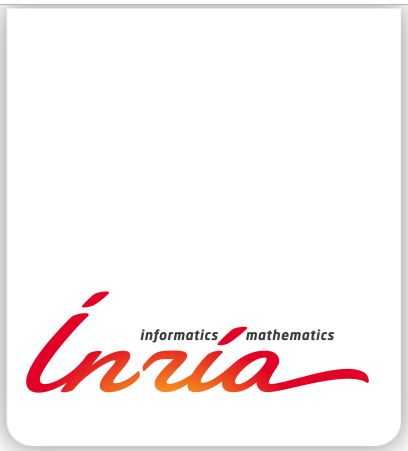

Irregular wave propagation with a 2DH Boussinesq-type model and an unstructured finite volume scheme

M. Kazolea*, A.I. Delis†

Project-Teams Cardamom

Research Report n° 9008 — December 2016 — 24 pages

Abstract: The application and validation, with respect to the transformation, breaking and run-up of irregular waves, of an unstructured high-resolution finite volume (FV) numerical solver for the 2D extended Boussinesq-type (BT) equations of Nwogu (1993) is presented. The numerical model is based on the combined FV approximate solution of the BT model and that of the nonlinear shallow water equations (NSWE) when wave breaking emerges. The FV numerical scheme satisfies the desired properties of well-balancing, for flows over complex bathymetries and in presence of wet/dry fronts, and shock-capturing for an intrinsic representation of wave breaking, that is handled as a shock by the NSWE. Several simulations and comparisons with experimental data show that the model is able to simulate wave height variations, mean water level setup, wave run-up, swash zone oscillations and the generation of near-shore currents with satisfactory accuracy.

Key-words: Irregular Waves, Boussinesq-type equations, Finite Volumes, Unstructured meshes

This is a note

This is a second note

* Inria Bordeaux Sud-Ouest, 200 Avenue de la Vielle Tour, 33405 Talence cedex, France- maria.kazolea@inria.fr
† School of Production Engineering and Management, Technical University of Crete, University Campus, Chania, Crete, Greece

RESEARCH CENTRE
BORDEAUX – SUD-OUEST

200 avenue de la Vieille Tour
33405 Talence Cedex

Propagation des vagues irrégulières avec un modèle Boussinesq 2DH et un schéma de volumes finis non-structurés

Résumé : On présente la validation d'un code Boussinesq non-structuré utilisant les equations de Nwogu sur simulation de la transformation et du déferlement de vagues correspondantes à des états de mer irréguliers. Le code résout les equations de Boussinesq par une méthode de type Volumes Finis (VF) avec une approximation de type Shallow-Water dans les régions déferlantes. Le schéma VF utilisé est well-balanced pour des bathymétries arbitraires et en présence de fronts secs. Les propriétés de capture de choc du schéma utilisé permettent aussi de représenter correctement les fronts déferlants par des ressauts, grace à l'utilisation locale des équations shallow water. La comparaison avec une large base de données expérimentales démontre le potentiel de l'approche proposée pour prédire avec une précision satisfaisante les hauteurs d'eau, le setup, l'inondation et l'oscillation dans la région de swash.

Mots-clés : vagues irréguliers, equations de type Boussinesq, Volumes Finis, non-structuré

1 Introduction

Accurate simulations of near-shore hydrodynamics is of fundamental importance to marine and coastal engineering. Wind and swell gravity water waves propagate towards the coastline in groups of high- and low-frequency waves which shoal in shallow waters and eventually break on the beach. As such, near-shore hydrodynamics are strongly influenced by the evolution of both high- and low-frequency waves and their interactions. Due to their dispersive nature, these wave groups are transient and evolve in space and time leading to wave focusing that can potentially result to the formation of extreme or rogue waves. In addition to the formation of extreme waves, the focusing of wave energy, along with the wave height variation across the group, forces low-frequency long waves that propagate with the wave group. These group bound long waves may be amplified by continued forcing during shoaling of the short-wave groups in shallower water. In sufficiently shallow water, the short waves within the group break at different depths, leading to further long-wave forcing by the varying breakpoint position. The influence of low-frequency waves on the short wave field is important, as it has been suggested that their presence might lead to the de-saturation of the surf zone at short wave frequencies. Furthermore, low-frequency motions, which contribute significantly to surf and swash zone energy levels, are relevant to sediment mobility, harbor oscillations, and coastal inundation.

Important physical effects associated with nonlinear transformations of sea waves in near-shore regions can be described by Boussinesq-type equations (BTE). BTE are more appropriate for describing flows in deeper waters where frequency dispersion effects may become more important than nonlinearity by introducing dispersion terms in the modeling thus being more suitable in waters where dispersion begins to have an effect on the free surface. Over the last decades, BTE have been widely used to describe wave transformations in coastal regions. For very recent comprehensive reviews on the theory, numerics and applications of BT models we refer to the review works in [8, 24]. The success of the BTEs is mainly due to the optimal blend of physical adequacy, in representing all main physical phenomena, and to their relative computational ease. However, the accurate and efficient numerical approximation of BT equations is still in the focus of on-going research especially in terms of higher-order numerics and the adaptive mathematical/numerical description of the flow. The first set of extended BTE was derived by Peregrine [34], under the assumption that nonlinearity and frequency dispersion are weak and they are limited to relatively shallow water due to the weak dispersion. Subsequent attempts to extent the validity and applicability of these so-called standard Boussinesq equations have been successful. Madsen and Sorensen [29] and Nwogu [33] have extended their validity by giving a more accurate representation of the phase and group velocities in intermediate waters, closely relating to linear wave theory. Furthermore, significant effort has been made in recent years into advancing the nonlinear and dispersive properties of BT models by including high order nonlinear and dispersion terms, we refer to [24] and references therein, which in turn are more difficult to integrate and thus require substantially more computational effort in their numerical integration. Further, the correct representation of the low-frequency wave generation and evolution is a requirement for near-shore simulation models. To this end, the achievement of a good modeling of low-frequency motion is closely related to an accurate simulation of nonlinear energy transfers, breaking-induced energy dissipation and swash zone motion; hence, an appropriate treatment of the wave breaking and wave run-up/run-down processes is very important.

The present work is complementary to [21, 22] where, for the first time, a high-order well-balanced unstructured finite volume (FV) scheme on triangular meshes was presented for modeling weakly nonlinear and weakly dispersive water waves over slowly varying bathymetries, as described by the 2D depth-integrated BTE of Nwogu [33]. The FV scheme numerically solves the conservative form of the equations following the median dual node-centered approach, for both the advective and dispersive part of the equations. For the advective fluxes, the scheme utilizes an approximate Riemann solver along with a well-balanced topography source term upwinding. Higher order accuracy in space and time is achieved through a MUSCL-type reconstruction technique and through a strong stability preserving explicit Runge-

Kutta time stepping. The model aims at combining the best features of the two families of equations: the propagation properties of Boussinesq equations and the shock-capturing features of the NSWE. At this purpose, it solves Boussinesq equations where nonlinear and dispersive effects are both relevant and NSWE where nonlinearity prevails and dispersion is negligible. To this end, a new methodology was presented in [22] to handle wave breaking over complex bathymetries in extended two-dimensional BT models. Certain criteria, along with their proper implementation, were established to characterize breaking waves. Once breaking waves are recognized, a switching is performed locally in the computational domain from the BTE to NSWE by suppressing the dispersive terms in the vicinity of the wave fronts. Thus, the shock-capturing features of the FV scheme enable an intrinsic representation of the breaking waves, which are handled as shocks by the NSWE. An additional methodology was presented on how to perform a stable switching between the BTE and NSWE within the unstructured FV framework The proposed approach is essential and has been proven efficient, especially in two dimensional conditions, for regular wave propagation. Since the model is intended for practical, engineering purposes it aims at accurately simulating the global effects of wave-breaking i.e. wave height decay, mean water level setup, current generation. Hence, the proposed model's its application and validation, with respect to the transformation, breaking and run-up of irregular waves is the main scope of this presentation

2 Mathematical Model

The model equations solved in the present work, following [21, 22], are the extended BT equations of Nwogu [33] which describe weakly non-linear weakly dispersive water waves in variable bathymetries. They were derived under the assumption that the wave height (A) to constant water depth (h) ratio, $\epsilon := A/h$, which measures the weight of nonlinear effects, and the square water depth to wave length (L) ratio $\mu^2 := h^2/L^2$, which represents the dimension of the dispersive effects, is of the same order with, i.e. the Stokes number $S := \epsilon/\mu^2 = O(1)$. The equations provide accurate linear dispersion and shoaling characteristics for values of kh up to 3 (intermediate water depths), where k is the wave number and kh is essentially a scale of the value of μ, providing a correction of $O(\mu^2)$ to the shallow water theory. By retaining $O(\mu^2)$ terms in the derivation of the models some vertical variations in the horizontal velocity are included even though the explicit appearance of the vertical coordinate has been removed from the continuity and momentum equations by integration.

Using the velocity vector $[u, v]^{\mathrm{T}} = \mathbf{u} \equiv \mathbf{u}_a$ at an arbitrary distance, z_a, from the still water level, h, as the velocity variable, an optimum value of $z_a = -0.531h$ is derived so that the dispersion properties of the equations most closely approximate those defined by linear wave theory, making the equations applicable to a wider range of water depths compared to the classical Boussinesq equations. Following [21] the vector conservative form of the equations reads as:

$$\partial_t \mathbf{U} + \nabla \cdot \mathcal{H}(\mathbf{U}^\star) = \mathbf{S} \quad \text{on} \quad \Omega \times [0, t] \subset \mathbb{R}^2 \times \mathbb{R}^+, \tag{1}$$

where $\Omega \times [0, t]$ is the space-time Cartesian domain, $\mathbf{U}^\star = [H, q_x, q_y]^{\mathrm{T}} = [H, Hu, Hv]^{\mathrm{T}}$ are the physically conservative variables, with H being the total water depth and $\mathbf{q} = [q_x, q_y]^{\mathrm{T}}$ are the volume fluxes along the x and y directions, $\mathbf{U}$ is the vector of the actual solution variables and $\mathcal{H} = [\mathbf{F}, \mathbf{G}]$ the nonlinear flux vectors given as

$$\mathbf{U} = \begin{bmatrix} H \\ P_1 \\ P_2 \end{bmatrix}, \quad \mathbf{F} = \begin{bmatrix} q_x \\ q_x^2/H + \dfrac{1}{2} g H^2 \\ q_x q_y / H \end{bmatrix}, \quad \mathbf{G} = \begin{bmatrix} q_y \\ q_x q_y / H \\ q_y^2/H + \dfrac{1}{2} g H^2 \end{bmatrix},$$

where

$$\mathbf{P} = \begin{bmatrix} P1 \\ P2 \end{bmatrix} = H \left[\frac{z_a^2}{2} \nabla(\nabla \cdot \mathbf{u}) + z_a \nabla(\nabla \cdot h\mathbf{u}) + \mathbf{u} \right]. \tag{2}$$

The source term vector, $\mathbf{S} = \mathbf{S}_b + \mathbf{S}_f + \mathbf{S}_d$, includes the bed topography's, $b(x, y)$, slope $\mathbf{S}_b$, the bed friction effects $\mathbf{S}_f$, and the dispersive terms $\mathbf{S}_d$. These terms read as

$$\mathbf{S}_b = \begin{bmatrix} 0 \\ -gH\partial_x b \\ -gH\partial_y b \end{bmatrix}, \quad \mathbf{S}_d = \begin{bmatrix} -\psi_c \\ -u\psi_c + \psi_{M_x} \\ -v\psi_c + \psi_{M_y} \end{bmatrix}.$$

with

$$\psi_c = \nabla \cdot \left[\left(\frac{z_a^2}{2} - \frac{h^2}{6} \right) h\nabla(\nabla \cdot \mathbf{u}) + \left(z_a + \frac{h}{2} \right) h\nabla(\nabla \cdot h\mathbf{u}) \right], \tag{3}$$

and

$$\boldsymbol{\psi}_M = \begin{bmatrix} \psi_{M_x} \\ \psi_{M_y} \end{bmatrix} = \partial_t H \frac{z_a^2}{2} \nabla(\nabla \cdot \mathbf{u}) + \partial_t H z_a \nabla(\nabla \cdot h\mathbf{u}). \tag{4}$$

The bed friction effects are approximated by the quadratic law:

$$\mathbf{S}_f = \begin{bmatrix} 0 \\ -\frac{f_w}{2} q_x \|\mathbf{q}\| h^{-2} \\ -\frac{f_w}{2} q_y \|\mathbf{q}\| h^{-2} \end{bmatrix}$$

where f_w is the bed friction coefficient, typically in the range of $O(10^{-3})$ to $O(10^{-2})$, depending on the Reynolds number and the bed material.

Equations (1) have flux terms identical as those in the NSW equations and variables $\mathbf{P}$ contain all time derivatives in the momentum equations, including part of the dispersion terms. The dispersion vector $\mathbf{S_d}$ contains only spatial derivatives since $\partial_t H$ is explicitly defined by the mass equation. It is obvious that the NSW equations are a subset of the BT equations since equations (1) degenerate into the NSW equations when the dispersive terms in $\mathbf{P}$ and $\mathbf{S}_d$ are vanishing.

2.1 Wave generation

The internal generation of wave motion is performed following the approach of Wei et al. [51]. The method employs a source term added to the mass equation. This source function was obtained using Fourier transform and Green's functions to solve the linearized and non-homogeneous equations of Peregrine and Nwogu. In the present model, this source function wave making method is adopted in order to let the reflected waves outgo through the wave generator freely.

To obtain a desired oscillation signal in the wave generating area, a source function $S(\mathbf{x}, t)$ is added into the mass conservation equation at each time step, which is expressed as

$$S(\mathbf{x}, t) = D^* \exp\left(\sigma(x - x_s)^2\right) \sin(\lambda y - \omega t) \tag{5}$$

in which

$$\sigma = \frac{5}{(\delta L/4)^2} = \frac{80}{\delta^2 L^2} \tag{6}$$

where L is the wave length, ω the wave frequency, θ the wave incident angle, $\lambda (= k_y = k \sin\theta)$ the wave number in the $y-$direction, x_s is the location of the center of the wave-making area, δ is a parameter that influences the width $W = \delta L/2$ of the wave generator area and D^* is the source function's amplitude. For a monochromatic wave, D^* is defined as

$$D^* = \frac{2\sqrt{\sigma} A_0 \cos\theta \left(\omega^2 - \alpha_1 g k^4 h^3\right)}{\omega k \sqrt{\pi} \exp(-l^2/4\sigma) \left[1 - \alpha(kh)^2\right]} \tag{7}$$

where h is again the still water level at the wave generation region, A_0 the wave amplitude, $l(= k_x = k\cos\theta)$ the wave number in the $x-$direction, $\alpha = -0.390$ and $\alpha_1 = \alpha + 1/3$.

For irregular waves and following [19] we use the linear superposition of component waves. According to the irregular wave concept of Longuet-Higgings et al. [27] the water surface elevation can be described by

$$\eta(t) = \sum_{i=1}^{\infty} a_i \cos(\omega_i t + \epsilon_i)$$

where, a_i and ω_i represent the amplitude and frequency of the component wave respectively and ϵ_i denotes the initial phase of the component wave, which is distributed randomly in the range of $[0, 2\pi]$. This means that each component wave has its deterministic amplitude and frequency. The source function now reads as:

$$S(\mathbf{x}, t) = \exp\left(\sigma(x - x_s)^2\right) \sum_{i=1}^{M} D_i^* \sin(\lambda_i y - \omega_i t + \epsilon_i) \tag{8}$$

where the source function's amplitude is now

$$D_i^* = \frac{2\sqrt{\sigma} A_i \cos\theta_i \left(\omega_i^2 - \alpha_1 g k_i^4 h^3\right)}{\omega k_i \sqrt{\pi} \exp(-l_i^2/4\sigma)\left[1 - \alpha(k_i h)^2\right]} \tag{9}$$

with $l_i = k_i \sin(\theta_i)$. For the wave making area W we use the maximum wavelength between the components.

The BT equations of Nwogu that we use in this work are restricted to h/L values less than $1/2$.. More precisely using a value of $\alpha = -0.39$ in the range $0 < h/L < 1/2$ gives an error of the normalised phase speed of less than 2% [33]. Beyond this range errors in the linear dispersion relationship grow, hence one should be careful when testing to accurately represent the free waves at the given frequency. Following [47, 30] the wave generator is placed, each time, at the position with the appropriate water depth.

3 The Numerical Methodology

To numerically solve BT system (1), the high-resolution shock-capturing finite volume (FV) scheme proposed in [21, 22] has been implemented. We will briefly review it here, for completeness. The considered FV approach is of the vertex-centered median-dual type where the control volumes are elements dual to a primal triangulation of the computational domain Ω. Referring to Fig. 1, the boundary ∂C_P of a computational cell C_P, around an internal vertex P, is defined by connecting the barycenters of the surrounding triangles with the mid-points of the corresponding edges that meet at vertex P.

After integration of (1) over each computational cell and application of the Gauss divergence theorem the semi-discrete form of the scheme follows the usual FV formulation and reads as

$$\frac{\partial \mathbf{U}_P}{\partial t} = -\frac{1}{|C_P|} \sum_{Q \in K_P} \widetilde{\boldsymbol{\mathcal{F}}}_{PQ} - \frac{1}{|C_P|} \widetilde{\boldsymbol{\mathcal{F}}}_{P,\Gamma} + \frac{1}{|C_P|} \sum_{Q \in K_P} \left\{ \iint_{C_P.} \mathbf{S}\, d\Omega \right\}, \tag{10}$$

where $\mathbf{U}_P$ is the volume-average value of the conserved-like quantities at a given time, K_P is the set of neighboring vertices to P, Γ is the boundary of Ω and $\widetilde{\boldsymbol{\mathcal{F}}}_{PQ}$ and $\widetilde{\boldsymbol{\mathcal{F}}}_{P,\Gamma}$ are the numerical flux vectors across each internal and boundary face, respectively. Assuming a uniform distribution of $\mathcal{H}$ over ∂C_{PQ}, equal to its value at the midpoint M of edge PQ, these fluxes are approximated as

$$\widetilde{\boldsymbol{\mathcal{F}}}_{PQ} = \oint_{\partial C_{PQ}} \left(\mathbf{F}\tilde{n}_x + \mathbf{G}\tilde{n}_y\right) dl \approx \left(\mathbf{F}\tilde{n}_x + \mathbf{G}\tilde{n}_y\right)_M \left\|\mathbf{n}_{PQ}\right\| = \left(\mathbf{F}n_{PQx} + \mathbf{G}n_{PQy}\right)_M. \tag{11}$$

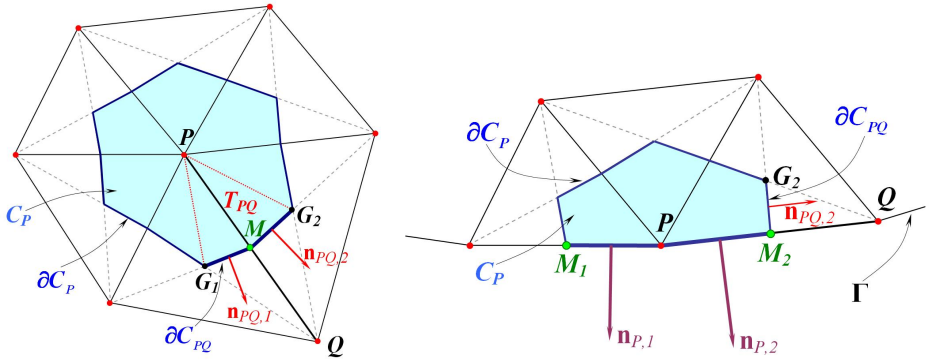

Figure 1: Median-dual computational cell definition (left) and boundary cell definition (right)

where $\tilde{\mathbf{n}} = [\tilde{n}_x, \tilde{n}_y]$ is the unit outward normal vector to the boundary Ω and $\mathbf{n}_{PQ} = [n_{PQx}, n_{PQy}]$ is the outward normal vector to the common face of the cells C_P and C_Q. To evaluate the product $\mathbf{F}n_{PQx} + \mathbf{G}n_{PQy}$ at M, a one dimensional Riemann problem is assumed, between the left and right states existing at the two sides of M, defined by the vectors $\mathbf{U}^{\star L}_{PQ}$ and $\mathbf{U}^{\star R}_{PQ}$ respectively. The numerical fluxes (11) in (10) were evaluated by the popular approximate Riemann solver of Roe [36].

The above scheme is only first-order accurate if a constant distribution of the physical variables is assumed in each cell C_P, i.e. $\mathbf{U}^{\star L}_{PQ} = \mathbf{U}^{\star}_{P}$ and $\mathbf{U}^{\star R}_{PQ} = \mathbf{U}^{\star}_{Q}$. For BT models higher-order accuracy of the first-order derivatives is required so that the truncation errors in the numerical scheme are smaller than the dispersion terms present in the model. The MUSCL methodology of van Leer [49], extended to the node-centered unstructured formulation, has been adopted as to achieve higher-order spatial accuracy. To this extend, the numerical fluxes are evaluated by linearly extrapolated $\mathbf{U}^{\star R}_{PQ}$ and $\mathbf{U}^{\star L}_{PQ}$ values at the midpoint M of edge PQ, using extrapolation gradients obtained using a combination of centered and upwind gradients [13, 21, 1, 40]. In that way, a third-order-accurate upwind-biased scheme is constructed, reducing the numerical dissipation introduced to the numerical fluxes computation. Following [2, 3, 4], the average of the gradient $(\nabla w)_P$ in a cell, which is necessary for the higher-order reconstruction and for the discretization of the dispersion terms later on, is computed in the region Ω_P which is described by the union of all triangles which share the vertex P. Thus, for a vertex P it holds that

$$(\nabla w)_P = \frac{1}{|C_P|} \sum_{Q \in K_P} \frac{1}{2}\Big(w_P + w_Q\Big)\mathbf{n}_{PQ}. \tag{12}$$

The integral average of the divergence of the velocity vector is computed applying again the divergence theorem and by approximating the line integrals using the trapezoidal quadrature rule, [21], leading to

$$(\nabla \cdot \mathbf{u})_P = \frac{1}{|C_P|} \sum_{Q \in K_P} \frac{1}{2}(\mathbf{u}_P + \mathbf{u}_Q) \cdot \mathbf{n}_{PQ}. \tag{13}$$

Further, in cases were the nonlinearity prevails, and as such the dispersion terms are negligible (e.g. when the NSWE are solved), the use of a slope limiting procedure is necessary as to reduce oscillations and new extrema that can appear around shocks. In this work, the edge-based nonlinear slope limiter of Van Albada-Van-Leer is used [1, 13, 17, 40, 48]. Details for the applied MUSCL-type reconstruction can be found in [21, 13].

To obtain a well-balanced FV scheme, an upwind discretization approach for the bed topography source term is adopted to satisfy the so-called $C-$property in hydrostatic (flow at rest) conditions [7, 20,

32]. To this end, the topography source term, $\mathbf{S}_b$ must be linearized in the same way and evaluated in the same Roe-average states as the flux terms. More details can be found in [21, 22]. Moreover, in wet/dry fronts special considerations are needed to accurately model transition between wet and dry areas and maintain the high-order spatial accuracy and mass conservation. As identified in [35, 13, 21], and we briefly list here for completeness, the following issues have are addressed:

- *Dry cell identification.* Computational cells with water depth $H < \epsilon_{wd}$ are considered as dry, where ϵ_{wd} is a tolerance parameter computed from grid geometrical quantities [35, 13].
- *Conservation of flow at rest with dry regions.* A FV scheme has to satisfy the extended C-property [11]. We redefine the bed elevation at the emerging dry cell following [12, 9, 32, 13, 10] to obtain an exact balance at the front between the bed slope and the hydrostatic terms for steady conditions.
- *Consisted depth reconstruction in dry regions.* In a wet/wet steady case, in each computational cell were the MUSCL reconstruction for b involves dry cells $(\nabla H)_P = -(\nabla b)_P$ must be inforced to maintain higher-order accuracy [13].
- *Flow in motion over adverse slopes.* For flow in motion and at wet/dry fronts we impose, temporarily, $\mathbf{u} = \mathbf{0}$ for the computation of the numerical fluxes and source terms, following [11, 12, 32].
- *Water depth positivity and mass conservation.* To avoid computing negative water depths in drying cells and to achieve absolute mass conservation, we follow treatments proposed in [9, 26, 13].

For the discretisation of the dispersion terms we assume a uniform distribution of the integrated quantities over ∂C_{PQ} equal to their values at the midpoint M of the edge PQ. The mass equation in (1) contains the integral average of the dispersive term ψ_C and to approximate this term, we use the divergence theorem, which leads to

$$(\psi_c)_P \approx \frac{1}{|C_P|} \sum_{Q \in K_P} \left\{ \left[\left(\frac{z_a^2}{2} - \frac{h^2}{6} \right) h \right]_M \left[\nabla(\nabla \cdot \mathbf{u}) \cdot \mathbf{n}_{PQ} \right]_M + \left[\left(z_a + \frac{h}{2} \right) h \right]_M \left[\nabla(\nabla \cdot h\mathbf{u}) \cdot \mathbf{n}_{PQ} \right]_M \right\}. \tag{14}$$

In (14) we require the evaluation of the gradient of the divergence of $\mathbf{u}$ and $h\mathbf{u}$ along the edge midpoints M. Hence, the evaluation of the gradient of a quantity w at M requires the definition of a new computational cell constructed by the union of the two triangles which share edge PQ. By denoting with $K_{PQ} := \{R \in \mathbb{N} \mid R \text{ is a vertex of } M_{PQ}\}$ we obtain

$$(\nabla w)_M = \iint_{M_{PQ}} \nabla w d\Omega = \oint_{\partial M_{PQ}} w \tilde{\mathbf{n}}_{RQ} dl = \sum_{\substack{R,Q \in K_{PQ} \\ RQ \in \partial M_{PQ}}} \frac{1}{2} (w_R + w_Q) \mathbf{n}_{RQ}, \tag{15}$$

with $\mathbf{n}_{RQ}$ the vector normal to the edge RQ.

Next, for the the dispersive source terms in the momentum equations we have

$$\frac{1}{|C_P|} \iint_{C_P} -\mathbf{u}\psi_c + \boldsymbol{\psi}_M d\Omega = -\mathbf{u}_P \iint_{C_P} \psi_c d\Omega + \frac{1}{|C_P|} \iint_{C_P} \boldsymbol{\psi}_M d\Omega. \tag{16}$$

The first term of the right hand side of the equation is discretized as before in (14) and the second term takes the discrete form:

$$\begin{aligned} (\boldsymbol{\psi}_M)_P = \frac{1}{|C_P|} \iint_{C_P} \boldsymbol{\psi}_M d\Omega &= \frac{1}{|C_P|} \iint_{C_P} \partial_t H \frac{z_a^2}{2} \nabla(\nabla \cdot \mathbf{u}) + \partial_t H z_a \nabla(\nabla \cdot h\mathbf{u}) d\Omega \\ &\approx \left[\partial_t H \frac{z_a^2}{2} \right]_P |C_P| \left[\nabla(\nabla \cdot \mathbf{u}) \right]_P + \left[\partial_t H z_a \right]_P |C_P| \left[\nabla(\nabla \cdot h\mathbf{u}) \right]_P, \end{aligned} \tag{17}$$

where the divergence $(\nabla \cdot \mathbf{u})_P$ and $(\nabla \cdot h\mathbf{u})_P$ are computed again using formula (12).

Concerning the time discretization, an optimal third order explicit Strong Stability-Preserving Runge-Kutta (SSP-RK) method was adopted [43, 21] under the usual CFL stability restriction. After each time step in the RK scheme, the values of the velocities $\mathbf{u} = [u, v]^{\mathrm{T}}$ must be extracted from the new solution variable $\mathbf{P} = [P_1, P_2]^{\mathrm{T}}$, from the momentum equation. The discretization of $\mathbf{P}$ results into a linear system $\mathbf{MV} = \mathbf{C}$ with $\mathbf{M} \in \mathbb{R}^{2N\times 2N}$, $\mathbf{V} = [\mathbf{u}_1, \mathbf{u}_2, \cdots \mathbf{u}_N]^{\mathrm{T}}$ and $\mathbf{C} = [\mathbf{P}_1, \mathbf{P}_2, \cdots \mathbf{P}_N]^{\mathrm{T}}$. Matrix $\mathbf{M}$ is a sparse, mesh dependent and structurally symmetric. Keeping in mind that $\mathbf{u}$ is our unknown velocity vector at each mesh node, each two rows of the matrix correspond to a vertex $P \in \{1, 2, \ldots, N\}$ on the grid and for each such vertex equation (2) holds. Using (12) to discretize equation (2) and replacing the arithmetic average in equation (12) by the values at the midpoints M of the edges equation (2) reads as:

$$H_P \left[\frac{(z_a^2)_P}{2} \frac{1}{|C_P|} \sum_{Q\in K_P} (\nabla \cdot \mathbf{u})_M \mathbf{n}_{PQ} + \frac{(z_a)_P}{|C_P|} \sum_{Q\in K_P} (\nabla \cdot h\mathbf{u})_M \mathbf{n}_{PQ} + \mathbf{u}_P \right] = \mathbf{P}_P. \tag{18}$$

After some calculations the sparse $2N \times 2N$ linear system to be solved can be presented in a compact form, as:

$$\frac{(z_a^2)_P}{2|C_P|} \sum_{Q\in K_P} (\mathbf{A}_Q \mathbf{u}_Q + \mathbf{A}_P \mathbf{u}_P) + \frac{(z_a)_P}{|C_P|} \sum_{Q\in K_P} (\mathbf{B}_Q \mathbf{u}_Q + \mathbf{B}_P \mathbf{u}_P) + \mathbf{I_2} \mathbf{u}_P = \frac{1}{H_P} \mathbf{P}_P, \; P = 1 \ldots N, \tag{19}$$

where the sub-matrices $\mathbf{A}_Q, \mathbf{A}_P, \mathbf{B}_Q, \mathbf{B}_P$, depend only on the geometric quantities $\mathbf{n}_{PQ}$ and area $|M_{PQ}|$.

The properties of the sparse matrix vary depending on the physical situation of each problem solved, the type of the grid used and the number of the nodes on the grid. The matrix was stored in the compressed sparse row (CSR) format of and linear system was solved using the Bi-Conjugate Gradient Stabilized method (BiCGStab) [38]. The ILUT pre-conditioner from SPARSKIT package [38] was implemented and the reverse Cuthill–McKee (RCM) algorithm [16] was also employed to reorder the matrix elements as to minimize the matrix bandwidth. Convergence to the solution was obtained in one or two steps for the test problems presented in following sections.

3.1 Wave breaking

For treating breaking waves the hybrid wave breaking model of Kazolea et al. [22] is implemented. This is a phase resolving model and up to now this treatment of breaking has only be tested on regular waves [15, 22]. It is based on a hybrid BT/NSWE approach [22, 46] meaning that when a wave breaking interface occurs, BTEs are turned into NSWE by switching off the dispersive terms. In this way, the wave breaking interface is treated as a bore by the NSWE and the shock capturing FV scheme. The model is described briefly below:

1. Using a new set of physical criteria we first estimate the location of breaking waves and then the NSWE are solved in the breaking regions and BTEs elsewhere. More precisely the criteria for triggering the wave breaking modeling within the FV scheme are

   - the surface variation criterion: $|\partial_t \eta| \geq \gamma \sqrt{gh}$
   - the local slope angle criterion: $\|\nabla \eta\|_2 \geq \tan(\phi_c)$, where ϕ_c is the critical front face angle at the initiation of breaking

   The first criterion flags for breaking when $\partial_t \eta$ is positive, as breaking starts on the front face of the wave and has the advantage that can be easily calculated during the running of the model. In previous works [15, 22] which studied regular wave breaking over complex bathymetries the value of γ varies from 0.35 to 0.65 and it may be affected by the scale of the wave under consideration.

Dealing with irregular wave breaking, it has been found, that these values are not affected. However, this criterion alone is inefficient for stably computing stationary (breaking or partially breaking) hydraulic jumps since in these cases $\partial_t \eta \approx 0$. The second criterion acts complementarily to the first one and is based on the critical front slope approach in [39, 41]. Depending on the BT model used and the breaker type, e.g. spilling or plunging, the critical slope values are in the range of $\phi_c \in [14^o,\ 33^o]$. For certain BT models this has been considered as the least sensitive breaking threshold, with the correct breaking location predicted for $\phi_c \approx 30^o$, see for example [28, 44], and is is the value adopted in this work. This value for ϕ_c is relatively large for this criterion to trigger the breaking process by its own in our BT model but is sufficient to detect breaking hydraulic jumps thus, correcting the limitation of the first criterion.

2. If at least one of the criteria is satisfied: we flag the relative solution nodes as breaking ones in the computational mesh..

3. We distinguish the different breaking waves by creating a dynamical list that contains the breaking nodes of such a wave and the different breaking waves are treated individually.

4. The wave front of each breaking wave is then handled as a bore by the NSWE dissipating energy. At the same time, we take into account that bores stop breaking when their Froude (Fr) number drops below a critical value. If $Fr \gg 1$ a bore is purely breaking and will consist of a steep front and if the Fr number drops below a certain value Fr_c non-breaking undular bores occur, see [44]. Thus, an additional criterion is needed to determine when to switch back to the BT equations for non-breaking bores, allowing for the breaking process to stop. The criterion adopted is based on the analogy between a broken wave and a bore in the sense of a simple transition between two uniform levels. The wave's Fr number is defined as:

$$Fr = \sqrt{\frac{(2H_2/H_1 + 1)^2 - 1}{8}}, \tag{20}$$

where H_1 is the water depth at the wave's trough and H_2 the water depth at the wave's crest. Since we have tracked each breaking wave individually (with its own dynamic list), it is relatively straightforward to find H_1 and H_2 for each wave. We simply approximate them by finding the minimum and maximum water depth respectively, from all the breaking nodes corresponding to that wave. If $Fr \leq Fr_c$ all the breaking points of that wave are un-flagged and the wave is considered non-breaking. Following [44, 22], the critical value for Fr_c was set equal to 1.3 in our computations.

5. For each breaking wave an extension of the computational region governed by the NSWE is performed, as to avoid non-physical effects that may appear at the interface between a zone governed by the BTEs and a zone governed by NSWE [22].

3.2 Boundary conditions

In the presented FV approach, the degrees of freedom are located directly on the physical boundary. As such, boundary conditions based on mesh faces rather than mesh vertices where adopted. To this end, the weak formulation was used where the boundary condition was introduced into the residual through the modified boundary flux $\widetilde{\mathcal{F}}_{P,\Gamma}$ in (5). The idea of using the weak formulation to calculate the flux (and dispersion terms) at the boundary has been used here in the description of wall (solid) boundary conditions [21].

Absorbing boundaries have also been applied which should dissipate the energy of incoming waves perfectly, in order to eliminate nonphysical reflections. In front of this kind of boundaries a sponge layer

is defined. On this layer, the surface elevation was damped by multiplying its value by a coefficient $m(\mathbf{x})$ defined as [52]

$$m(\mathbf{x}) = \sqrt{1 - \left(\frac{\mathbf{x} - d(\mathbf{x})}{L_s}\right)^2} \tag{21}$$

where L_s is the sponge layer width and $d(\mathbf{x})$ is the normal distance between the cell center with coordinates $\mathbf{x}$ and the adsorbing boundary. The sponge layer width should be $L \leq L_s \leq 1.5L$, i.e. the width of the sponge layer is proportional to the wave length. Thus, longer wave lengths require longer sponge layers.

4 Numerical Tests and Results

4.1 Bichromatic wave groups

The first test case reproduces the experiments made by Mase [31] on the transformation, breaking and run-up of bichromatic wave groups on a mildly sloping beach. Mase's laboratory measurements, which include shoaling, breaking and swash motion, can provide good test cases for the verification of a run-up scheme in combination with a wave breaking model. Subsequently, these test cases have been used by researchers, e.g. [47, 30, 23], to evaluate their numerical models.

In the experiments, waves were generated in a wave flume of $27m$ long and $0.5m$ wide. The irregular wave generator was installed at the left end of the flume and a mild slope beach of $(1/20)$ was placed at the opposite end. The toe of the beach is placed $10m$ far from the irregular wave generator, see Fig. 2. In the numerical experiment we consider a wave-flume with dimensions $(x, y) \in [-5,\ 21m] \times [0,\ 2.5m]$

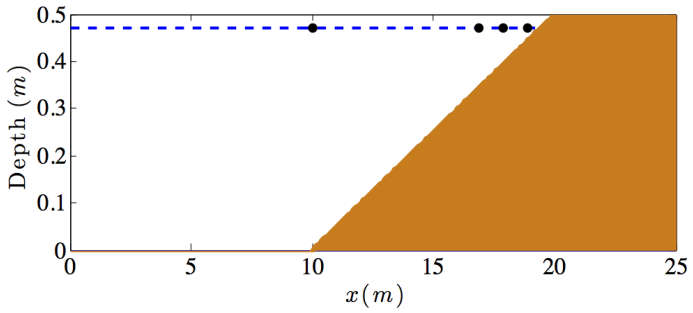

Figure 2: Topography description and position of the wave gauges (•) for the experiments by Mase [31].

and an undisturbed water depth $h = 0.47m$ at $x = 0m$. A triangular grid was used leading to a mesh with N=42,833 nodes with maximum length edge equal to 0.04m. Data from four wave gauges (WG) placed along the flume, namely those labeled 1 (placed at $x = 10m$), 8 (at $x = 16.9m$), 10 (at $x = 17.9m$) and 12 (at $x = 18.9m$), with WG 1 located at the toe of the sloping beach, were used in the present work. The wave generator was placed at $x = 0m$ with δ, the parameter which influences the width of the wave generator region, equals to 2.5. The γ value used in the wave breaking criterion was set in 0.6 and the CFL value used was 0.3. A sponge layer of $4m$ was placed at the left end of the domain as to absorb the wave energy and to prevent non-physical reflections from the closed boundary.

The bichromatic wave trains can be described by the equations:

$$\begin{aligned} \eta(t) &= A cos(2\pi f_1 t) + A cos(2\pi f_2 t) \\ f_{1,2} &= f_m \left(1 \pm \frac{1}{20}\right) \end{aligned} \tag{22}$$

where f_m is the mean frequency and A the wave's amplitude. In this work three different values of the mean frequency have been used that is $f_m = 1, 0.6$ and $0.3Hz$ and $a = 0.015m$ which leads to a medium energy level. Changing the mean frequency leads to a variation of the waves characteristics. As f_m is reduced the deep water wave steepness decreases and the probability that plunging breakers occur instead of spilling breakers is higher for low mean frequencies. An explanation of that is given in [47] using the surf similarity parameter defined by [5]. The first and the second case in this work use $f_m = 1Hz$ and $0.6Hz$ respectively where spilling wave breaking occurs, while the third test case uses $f_m = 0.3Hz$ where the wave breaker is mainly of the plunging type. Bed friction was neglected in these test cases and the wet/dry ϵ_{wd} tolerance parameter was set equal to 10^{-6}.

In order to produce the wave pattern, and since we use (8) we need the wave amplitude and frequency of each wave component as to define the source function amplitude (9). The numerical wave trains are generated internally using linear theory and following the bichromatic wave pattern given in (22), to identify the frequency components of the wave signal; however, as the actual experimental frequencies and amplitudes deviated from the target ones, several trials were necessary to find the best match with the measured waves. In [47] it is noted that in the experiments the generation of spurious harmonics was not compensated at the generator and that there was no active absorption of reflected waves, therefore it is difficult to reproduce the laboratory conditions exactly. After several trials we found the used mean frequencies for each case respectively: $f_m = 1.03,\ 0.605,\ 0.31Hz$

In Figs 3, 5 and 7 comparisons of the numerical and experimental time series of surface elevation recorded at specific wave gauge are presented for the different cases. Further, in Figs 4, 6 and 8, comparisons of the numerical and experimental measured time series of the vertical shoreline displacement for the run-up in the three test cases are presented.

Near the shoreline where wave breaking occurs, although slight discrepancies are observed, the overall agreement is satisfactory between the computed surface elevation and the experimental data. Moreover, the modeled swash motions are in good agreement with the measurements. The good agreement demonstrates that the present numerical model with its wave breaking model works reasonably well for the simulation of wave shoaling, breaking, and swash oscillation. it is important to note here that, in the numerical model, no special treatment is required at the shoreline, other than the conservative wet/dry front treatment described in Section 3 hence, swash zone oscillations are intrinsically represented by the model.

4.2 Irregular waves over a bar

Beji and Battjes [6] conducted multiple laboratory experiments to examine sinusoidal wave propagation over a sub-merged bar. Their purpose was to elucidate the phenomenon of high frequency energy generation observed in the power spectra of waves traveling over submerged bars. They studied both regular and irregular waves. The produced experimental data (especially those include the regular waves) has been used extensively in the literature for model validation, see for example [53, 37, 45, 21] among others. The experiments were conducted in a $37.7m$ long, $0.8m$ wide, and $0.75m$ high wave flume. They performed tests for both breaking and non-breaking waves. In this work one of the non-breaking test cases is reproduced. The peak frequency is $0.4Hz$ and the wave's amplitude is $2.9cm$. Irregular waves of a JONSWAP spectrum are introduced in the domain.

The bottom topography consisted by a submerged trapezoidal bar of 0.3 m high with a front slope of 1:20 and a lee slope of 1:10 separated by a level plateau 2 min length. To be able to apply $6.5m$ length sponge layers at the two ends of the domain and place the wave generator at $x = 0m$ the dimensions of the computational domain were set to $(x, y) \in [-10,\ 30] \times [0,\ 0.8m]$. For the computation a triangular grid was used, consisting of equilateral triangles with side length of 0.03 m, leading to a mesh of N=40,346 nodes. For this test case $\delta = 2.5$ and the CFL value used is 0.3. The free-surface elevations are recorded at eight gauges over and behind the bar as in the laboratory experiment. The definition of the computational

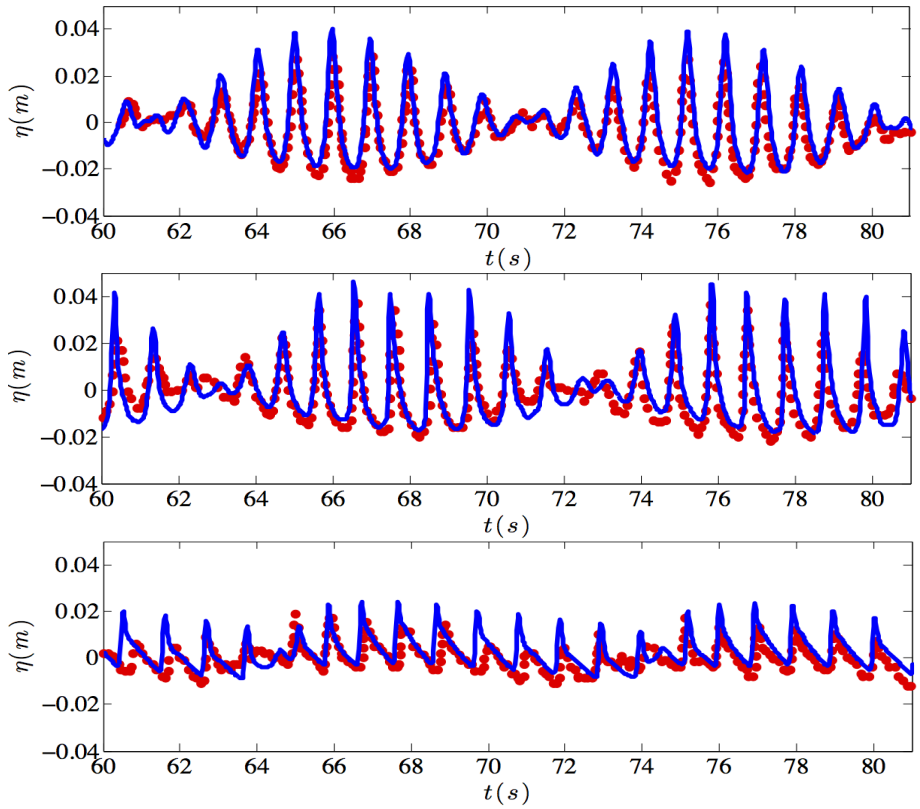

Figure 3: Comparison of time series of the surface elevation in the wave gauges 8, 10 and 12 (from top to bottom)) for bicromatic waves with $f_m = 1Hz$ between numerical solution (solid line) and experimental data.

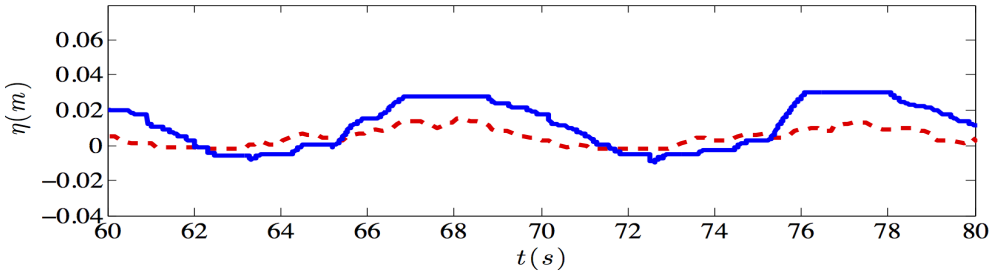

Figure 4: Comparison of the time series of the shoreline elevation for bicromatic wave trains produced with $f_m = 1Hz$ between the numerical (solid line) and the experimental (dashed line) one.

domain along the centerline as well as the wave gauge locations are shown in Fig. 9.

As mentioned above the wave gauges record the time series of the free surface elevation. The analysis of the collected data carried out with the usage of the standard FFT package WAFO [50]. The data segments, in each gauge, are 150s long. Fig. 10 shows the computed and experimental normalized energy spectrum for four wave gauges along the submerged bar. The numerical data slightly overestimate

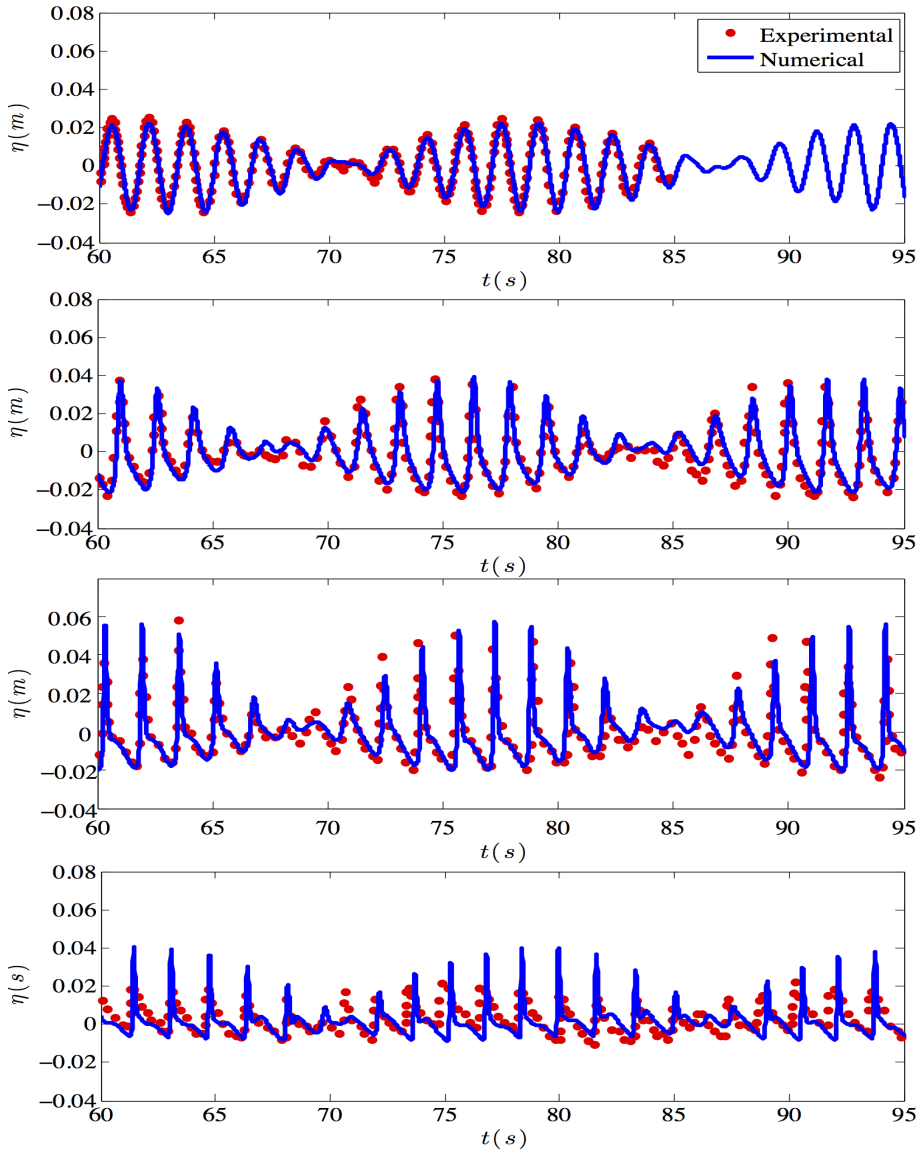

Figure 5: Comparison of time series of the surface elevation in the wave gauges 1, 8, 10 and 12 (from top to bottom)) for bicromatic waves with $f_m = 0.6Hz$ between numerical solution (solid line) and experimental data.

the spectral energy density, at the high frequency, especially at the gauges which are located at the lee side of the bar. It may be related to the inability of the equations to accurately resolve the breakup of the wave trains into independent waves due to the back slope. Bound higher harmonics are developed along the front slope which are then released from the carrier frequency on the lee side of the bar as the water depth parameter kh increases rapidly.

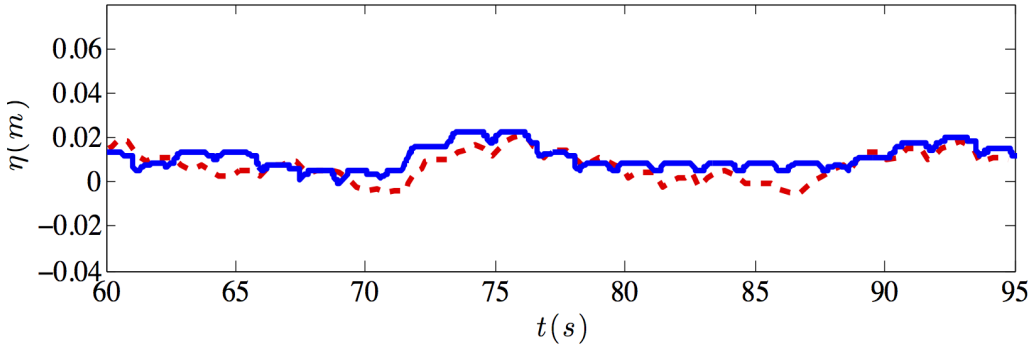

Figure 6: Comparison of the time series of the shoreline elevation for bicromatic wave trains produced with $f_m = 1Hz$ between the numerical (solid line) and the experimental (dashed line) one.

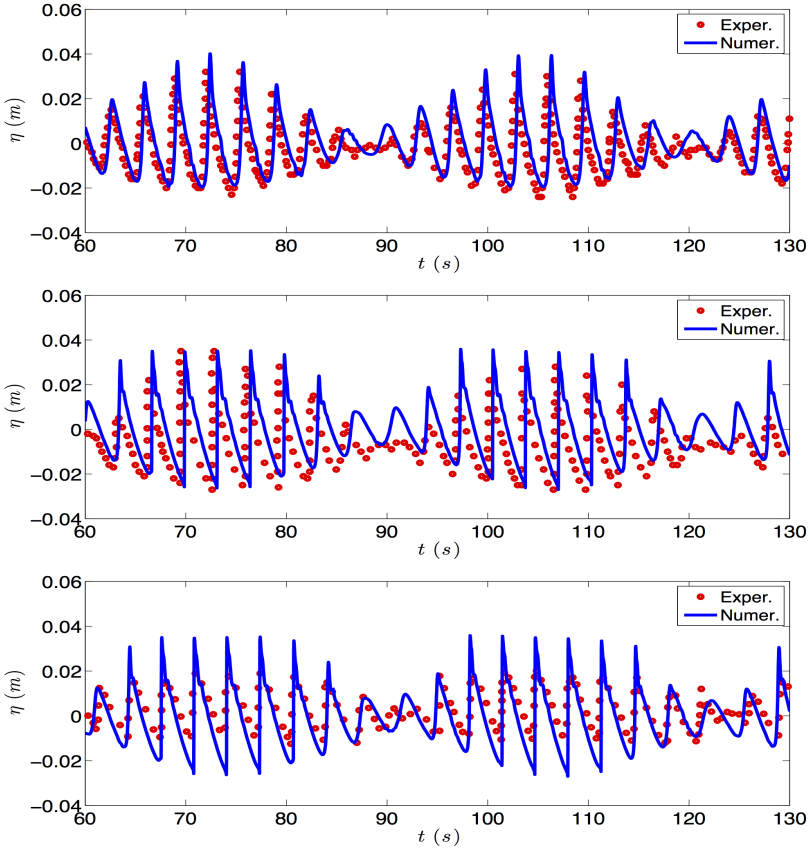

Figure 7: Comparison of time series of the surface elevation in the wave gauges 8, 10 and 12 (from top to bottom)) for bicromatic waves with $f_m = 0.3Hz$ between numerical solution (solid line) and experimental data.

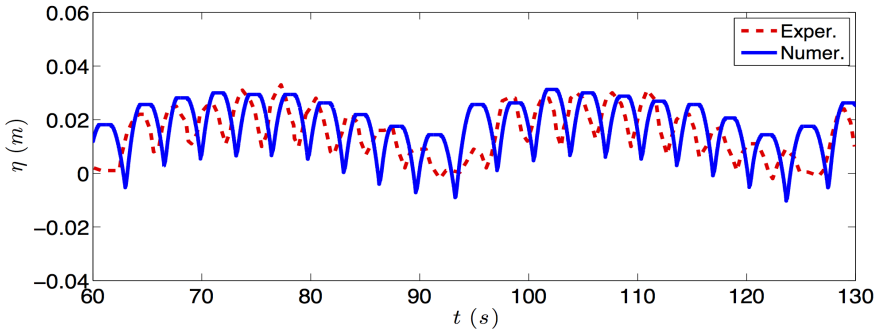

Figure 8: Comparison of the time series of the shoreline elevation for bicromatic wave trains produced with $f_m = 0.3Hz$ between the numerical (solid line) and the experimental (dashed line) one.

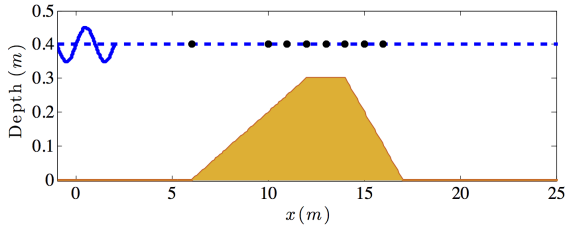

Figure 9: Topography description and position of the wave gauges (•)

4.3 Rip Current

The next test case reproduces the laboratory tests performed by Hamm [18]. This test has been used, for example in [47, 14, 42, 25], to test the ability of a model to reproduce wave propagation from deep water to the shore, including the surf zone, and breaking included nearshore circulation. More precisely, the nearshore circulation induced by breakers in the presence of a beach with a rip channel is numerically investigated. The physical domain used by Hamm was $30m \times 30m$ but in this work in order to save computational time and following [47], only half of the wave tank is modelled in the numerical domain and a fully reflective boundary condition is imposed at the centreline, which is the line of symmetry of the domain. The bottom topography is given as:

$$b(x,y) = \begin{cases} 0, & x \le 7; \\ 0.6 - \dfrac{25-x}{30}\left[1 + 3\exp(-\dfrac{25-x}{3})\cos^{10}\left(\pi\dfrac{15-y}{30}\right)\right], & 7 < x < 25; \\ 0.6 - \dfrac{25-x}{30}, & x \ge 25, \end{cases}$$

which consists of a horizontal bottom region of water depth 0.5 m followed by a plane sloping beach with a rip channel excavated along the centreline. Two experiments were reproduced in this work. The first one used monochromatic waves and the second one used an irregular wave pattern.

The dimension of the computational domain were set to $(x, y) \in [-3,\ 26]m \times [0,\ 15]m$. The triangular grid used, consisted of equilateral triangles with length of....leading to a mesh of N=50,721 nodes. The CFL number used was set to 0.3 and the internal wave generator, with δ value equal to 2.5, was set to $x = 0m$ for both cases. A sponge layer of 3m was placed on the offshore boundary. Fully reflective

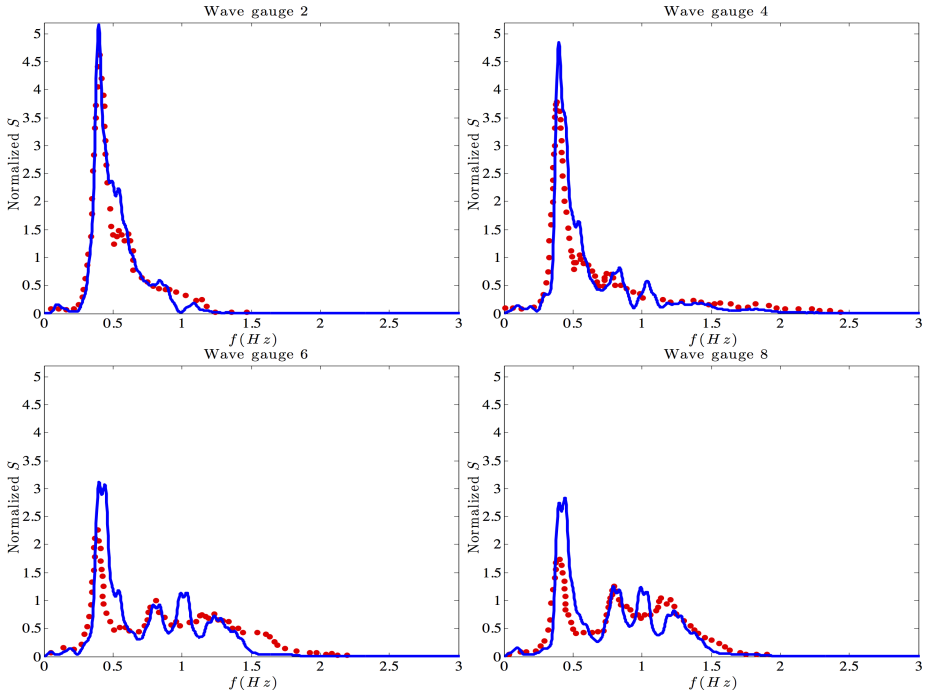

Figure 10: Power spectrum of the surface elevation for the wave gauges 2,4,6 and 8.

conditions used in the remaining boundaries. The simulated time was 520s.

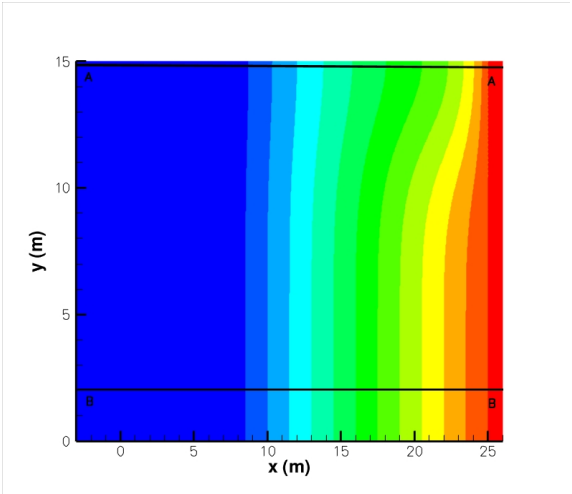

Figure 11: Topography and cross sections AA and BB for the rip current test case.

For the first test case a monochromatic wave is generated with an incident wave period of $T = 1.25s$ and wavelength $H = 0.07m$. A constant friction factor of $f_w = 0.03m$ is used in the bed friction term. In

the numerical simulation the regular waves are produced at $x = 3m$ and propagate towards the shore, shoal and break over the plane portion of the beach. The alongshore gradient in the mean water level which is formed due to the difference in the wave set-up along the rip channel and the plane beach, drives the formation of a current towards the centreline. Due to this current, and when it has been fully developed, the waves inside the rip, shoal and eventually break. The steady state current field is reached after 150s. Fig. 12 presents the mean water level set-up along with the mean current velocity field and a snapshot of the wave field at t=200s when the breaking induced circulations are fully developed. The velocity vectors are showed in a coarser grid every 0.5m. The velocity field reveals the rip current along the centreline of the bathymetry, i.e. at the right top of the figure. More precisely this figure shows the occurrence of an under-clockwise vortex, with its center approximately at $x = 22.5, my = 14m$. Fig. 13 shows the variation of the mean wave height H at the two cross-shore sections, one inside the rip channel ($y = 14.962m$) and one at the plane beach ($y = 1.985m$) (see Fig. 11). Also, the cross-shore variation of the mean current velocity is presented. The mean wave height at the two cross-shore sections have been obtained using the zero-up crossing technique.

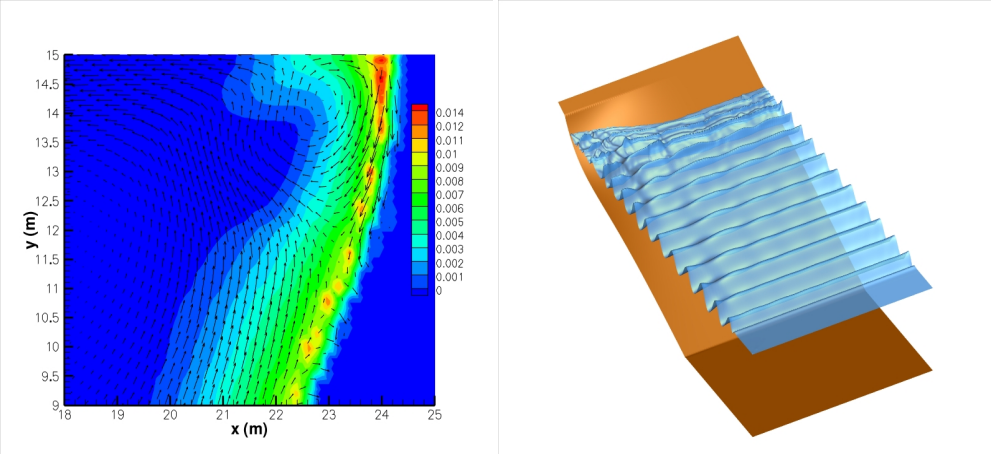

Figure 12: Mean water level set-up and mean velocity field (left), and snapshot of the free surface elevation for the monochromatic case (right).

The second test case includes the generation of irregular waves over the same topography. The generated wave spectrum corresponds to the Jonswap spectrum with an amplification factor $\gamma = 3.3$. The peak period is $T_p = 1.976s$ and the significant wave hight is $H_s = 0.04m$. Like before, the wave is generated at $x = 3m$ and a sponge layer of $4m$ is placed offshore. The friction factor f_w is reduced to 0.02 since both the current and the orbital wave velocities are weaker. The overall behaviour of the case is the same as before. The waves propagate onshore, shoal and the highest waves of the random wave train, break over the plane portion of the beach where the water depth is lower. The presence of the rip current makes the waves break at different positions in the cross-shore direction. The waves propagating over the linearly varying bathymetry break earlier than those propagating over the rip, where the water depth is higher. Different values of breaking induced wave set up cause gradients in mean water level elevation driving alongshore currents that turns offshore-ward producing the rip current at the channel location. Fig. 15 shows a vortex with the centre approximately at $x = 22.5, my = 14m$. Fig. 16 presents the variation of the significant wave height H_s along the two sections. The significant wave height has been obtained by a wave per wave analysis using the zero-down crossing technique. H_s is defined as the mean wave height (trough to crest) of the highest third of the waves $H_{1/3}$. Figure 17 shows the cross-shore variation of the

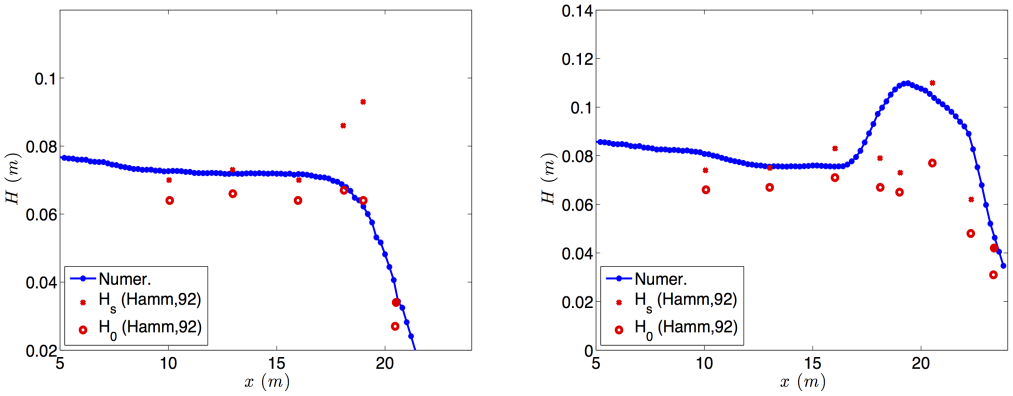

Figure 13: Cross-shore variation of the wave height H along the rip channel AA (left) and the plane beach BB sections (right) for the monochromatic wave case.

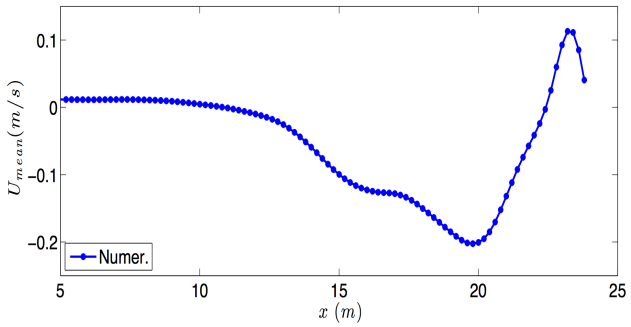

Figure 14: Cross-shore variation of the mean current velocity for the regular wave case.

mean velocity along the rip channel.

5 Conclusion

An unstructured finite volume (FV) scheme for the approximation of the extended 2D Boussinesq-type (BT) equations of Nwogu (1993) in the nearshore area was described. The scheme incorporates an approach to wave breaking based on the coupled solution of the BT equations and the nonlinear shallow water equations (NSWE). The proposed treatment is essential, but robust and efficient: thanks to the shock-capturing features of the FV scheme, the formation and evolution of breakers, and swash zone oscillations emerge as parts of the solution. The purpose of the paper consists in verifying the suitability of the numerical scheme for the simulation of irregular wave propagation, breaking and swash zone motion. The model was first validated against experimental from the evolution, breaking and runup of bichromatic wave groups on a mildly sloping beach. Good agreement was found; the model accurately reproduced shoreline motion and the transformation of the features of the swash oscillation with the breaking regime. Irregular waves propagation over a bar was then considered. The model was applied to simulate the laboratory test conducted and the numerical results were compared to the measured data. The model was

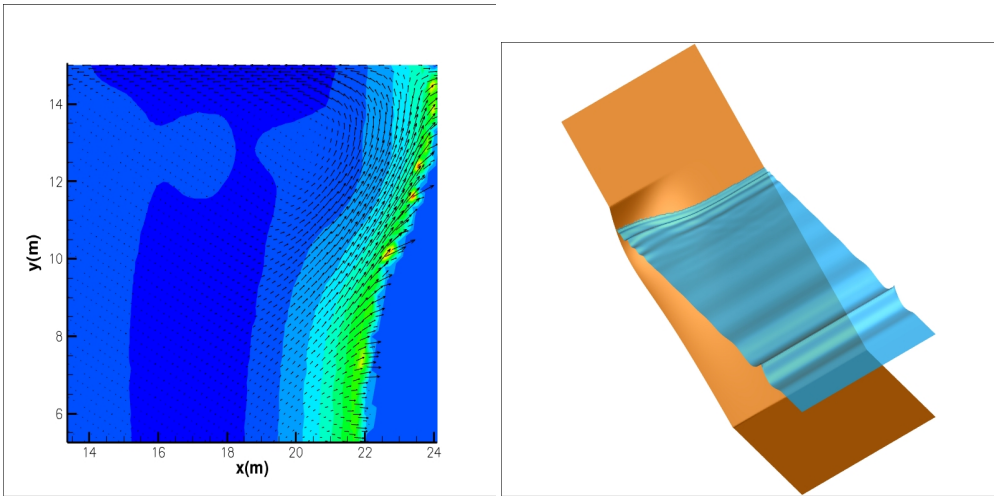

Figure 15: Mean water level set-up and mean velocity field (left), and snapshot of the free surface elevation (right) for the irregular test case.

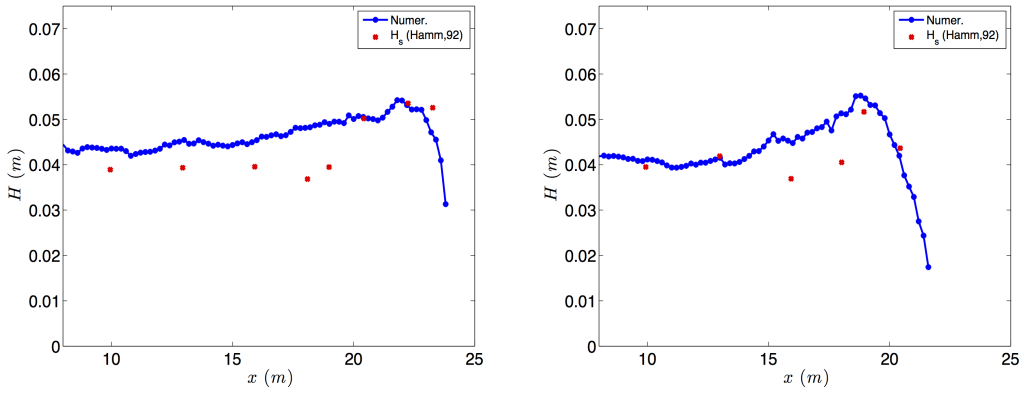

Figure 16: Cross-shore validation of the wave height H along the rip channel AA (left)and the plane beach BB (right) sections.

able to predict wave evolution and breaking, correctly reproducing the growth of low-frequency oscillations. Finally, a test case was performed to study regular and irregular wave transformation over a plane beach with a rip channel. The cross-shore transformation of wave heights and energy density spectra was appropriately modelled both over the slope and in the rip channel, indirectly testifying the accurate representation of wave breaking, mean water level setup and of the generation of a breaking-induced rip current. It is important to note that, given the limitations of the proposed BT equations, the numerical model cannot be expected to give a detailed description of wave shapes or velocity profiles at breaking but it aims at efficiently and accurately simulating its global effects (wave height decay, mean water level setup, current generation) which are the most important features for engineering applications. Under this point of view, good results were achieved, also for irregular wave propagation.

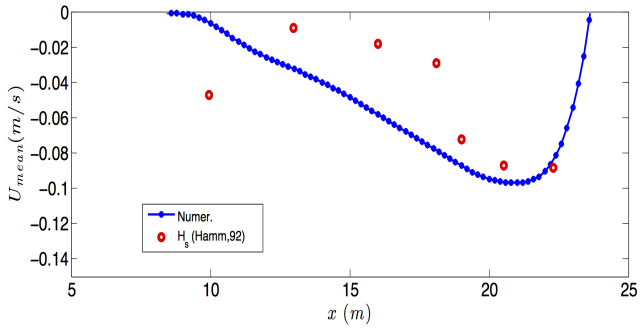

Figure 17: Cross-shore variation of the mean current velocity for the irregular wave case.

References

References

[1] T. J. Barth. A 3-D upwind Euler solver for unstructured meshes. *AIAA paper 91-1548CP*, 1991.

[2] T. J. Barth. Aspects of unstructured grids and finite volume solvers for the Euler and Navier-Stokes equations. In Special Course on Unstructured Grid Methods for advection Dominated Flows, AGARD report 787, 1992.

[3] T. J. Barth. *Numerical Methods and Error Estimation for Conservation laws on Structured and Unstructured Meshes*. VKI Computational Fluid Dynamics Lecture Series, 2003.

[4] T. J. Barth and M. Ohlberger. Finite volume methods: foundation and analysis. In E. Stein, R. de Borst, and T.R. Hudges, editors, *Encyclopedia of Computational Mechanics*. John Wiley and Sons Ltd., 2004.

[5] J. A. Battjes. Surf similarity. In *Proc. 14th Int. Conf. Coastal Eng*, pages 446–480, 1974.

[6] S. Beji and J. A. Battjes. Experimental investigations of wave propagation over a bar. *Coastal Eng.*, 19:151, 1993.

[7] A. Bermudez, A. Dervieux, J. A. Desideri, and M. E. Vázquez. Upwind schemes for the two-dimensional shallow water equations with variable depth using unstructured meshes. *Computer Methods in Applied Mechanics and Engineering*, 155(1-2):49, 1998.

[8] M. Brocchini. A reasoned overview on Boussinesq-type models: the interplay between physics, mathematics and numerics. *Proc. R. Soc. A*, 469 (20130496):dx.doi.org/10.1098/rspa.2013.0496, 2013.

[9] P. Brufau, P. García-Navarro, and M. E. Vázquez-Cendón. Zero mass error using unsteady wetting-drying coditions in shallow flows over dry irregular topography. *Int. J. Numer. Meth. Fluids*, 45:1047–1082, 2004.

[10] P. Brufau, M. E. Vázquez-Cendón, and P. Gracía-Navarro. A numerical model for the flooding and drying of irregular domain. *Int. J. Numer. Meth. Fluids*, 39:247, 2002.

[11] M. J. Castro, A. M. Ferreiro, J. A. García-Rodriguez, J. M. González-Vida, J. Macías, C. Parés, and M. E. Vázquez-Cendón. The numerical treatment of wet/dry fronts in shallow flows: Application to one-layer and two-layer systems. *Mathematical and Computer Modelling*, 42:419–439, 2005.

[12] A. I. Delis, M. Kazolea, and N. A. Kampanis. A robust high resolution finite volume scheme for the simulation of long waves over complex domain. *Int. J. Numer. Meth. Fluids*, 56:419–452, 2008.

[13] A. I. Delis, I. K. Nikolos, and M. Kazolea. Performance and comparison of cell-centered and node-centered unstructured finite volume discretizations for shallow water free surface flows. *Archives of Computational Methods in Engineering*, 18:57–118, 2011.

[14] Gallerano F., G. Cannata, and Villani M. An integral contravariant formulation of the fully non-linear boussinesq equations. *Coast. Eng.*, 83:119–136, 2014.

[15] A.G. Filippini, M. Kazolea, and M. Ricchiuto. A flexible genuinely nonlinear approach for nonlinear wave propagation, breaking and run-up. *Journal of Computational Physics*, 310:381–417, 2016.

[16] A. George and J. W. H Liu. *Computer solution of Large Sparce Positive Definite Systems*. Prentice Hall: Englewood Cliffs, N.J., 1981.

[17] E. Godlewski and P. A. Raviart. *Hyperbolic systems of conservation laws, Applied Mathematical Sciences, vol. 118*. Springer, Berlin, 1995.

[18] L. Hamm. Directional nearshore wave propagation over a rip channel: an experiment. In *Proc. 23rd Int. Conf. Coastal Eng.*, 1992.

[19] G. Hanbin, L. Yanbao, L. Shaowu, and Luwen Q. Applications of a boussinesq wave model. In *International Conference on Estuariew and Coasts*, 2003.

[20] M. E. Hubbard and P. García-Navarro. Flux difference splitting and the balancing of source terms and flux gradients. *J. Comp. Phys.*, 165:89–125, 2000.

[21] M. Kazolea, A. I. Delis, I. A Nikolos, and C. E. Synolakis. An unstructured finite volume numerical scheme for extended 2D Boussinesq-type equations. *Coast. Eng.*, 69:42–66, 2012.

[22] M. Kazolea, A. I. Delis, and C. E. Synolakis. Numerical treatment of wave breaking on unstructured finite volume approximations for extended Boussinesq-type equations. *J.Comput.Phys.*, 271:281–305, 2014.

[23] A. B. Kennedy, J .T. Chen, Q. Kirby, and R. A. Dalrymple. Boussinesq modeling of wave transformation, breaking and runup. Part I: 1D. *J. Waterw., Port, Coast., Ocean Engrg.*, 126:39–47, 2000.

[24] J.T. Kirby. Boussinesq models and their application to coastal processes across a wide range of scales. *Journal of Waterway, Port, Coastal and Ocean Engineering*, 142(6), 2016.

[25] G.T. Klonaris, C.D. Memos, and N.K. DrÃ¸nen. High-order boussinesq-type model for integrated nearshore dynamics. *Journal of Waterway, Port, Coastal and Ocean Engineering*, 142(6), 2016.

[26] Q. Liang and A. G. L. Borthwick. Adaptive quadtree simulation of shallow flows with wet/dry front over complex topography. *Comput. Fluids*, 38:221–234, 2009.

[27] M. S. Longet-Higgins, D. E. Cartwright, and N. D Smith. Observation of the directional spectrum of sea waves using the motions of a floating buoy. In *Proc. Conf. of Ocean Wave Spectra*, 1961.

[28] P. J. Lynett. Nearshore Wave Modeling with High-Order Boussinesq-Type Equations. *Journal of Waterway, Port, Coastal, and Ocean Engineering*, 132:348–357, 2006.

[29] P. A. Madsen and O. R. Sørensen. A new form of the Boussinesq equations with improved linear dispersion characteristics. Part 2: A slowing varying bathymetry. *Coast. Eng.*, 18:183–204, 1992.

[30] P.A. Madsen, O. R. Sørensen, and H. A. Schäffer. Surf zone dynamics simulated by a Boussinesq-type model: Part II. Surf beat and swash oscillations for wave groups and irregular waves. *Coast. Eng.*, 32:289–319, 1997b.

[31] H. Mase. Frequency down-shift of swash oscillations compared to incident waves. *J. Hydraulic Res*, 33:3:397–411, 1995.

[32] I. K. Nikolos and A. I. Delis. An unstructured node-centered finite volume scheme for shallow water flows with wet/dry fronts over complex topography. *Comput. Methods Appl. Mech. Engrg*, 198:3723–3750, 2009.

[33] O. Nwogu. An alternative form of the Boussinesq equations for nearshore wave propagation. *Journal of Waterway, Port, Coastal, and Ocean Engineering*, 119:618–638, 1994.

[34] D. H. Peregrine. Long waves on a beach. *J. Fluid Mech.*, 27:815–882, 1967.

[35] M. Ricchiuto and A. Bollermann. Stabilized residual distribution for shallow water simulations. *J.Comput.Phys*, 228:1071–1115, 2009.

[36] P. L. Roe. Approximate Riemann solvers, parameter vectors, and difference schemes. *J. Comp. Phys.*, 43:357–372, 1981.

[37] V. Roeber, K. F. Cheung, and M. H. Kobayashi. Shock-capturing Boussinesq-type model for nearshore wave processes. *Coast. Eng.*, 57:407–423, 2010.

[38] Y. Saad. *Iterative Methods for Sparse Linear Systems*. PWS, 1996.

[39] H. A. Schäffer, P.A. Madsen, and R. Deigaard. A Boussinesq model for waves breaking in shallow water. *Coast. Eng.*, 20:185–202, 1993.

[40] T. M. Smith, M. F. Barone, and R. B. Bond. Comparison of reconstruction techniques for unstructured mesh vertex centered finite volume schemes. *18th AIAA Computational Fluid Dynamics Conference*, pages 1–22, 2007.

[41] O. R. Sørensen, H. A. Schäffer, and P. A. Madsen. Surf zone dynamics simulated by a Boussinesq type model: Part III. Wave-induced horizontal nearshore circulations. *Coastal. Eng.*, 33:155–176, 1998.

[42] O. R. Sørensen, H.A. Shäffer, and L.S. Sørensen. Boussinesq-type modelling using an unstructured finite element technique. *Coastal Eng.*, 50:182, 2004.

[43] R. J. Spiteri and S. J. Ruuth. A new class of optimal high-order strong-stability-preserving time discretization methods. *SIAM J. Numer. Anal.*, 40:469, 2002.

[44] M. Tissier, P. Bonneton, F. Marche, F. Chazel, and D. Lannes. A new approach to handle wave breaking in fully non-linear Boussinesq models. *Coastal Engineering*, 67:54–66, 2012.

[45] M. Tonelli and M. Petti. Hybrid finite-volume finite-difference scheme for 2DH improved Boussinesq equations. *Coast. Eng.*, 56:609–620, 2009.

[46] M. Tonelli and M. Petti. Finite volume scheme for the solution of 2D extended Boussinesq equations in the surf zone. *Ocean. Eng.*, 37:567–582, 2010.

[47] M. Tonelli and M. Petti. Shock-capaturing Boussinesq model for irregular wave propagation. *Coastal Engineering*, 61:8–19, 2012.

[48] G. D. Van Albada, B. Van Leer, and W. W. Roberts. A comparative study of computational methods in cosmic gas dynamics. *Astron. Astrophysics*, 108:46–84, 1982.

[49] B. van Leer. Towards the ultimate conservative difference scheme V. A second order sequel to Godunov's method. *J. Comp. Phys.*, 32:101, 1979.

[50] WAFO-group. *WAFO - A Matlab Toolbox for Analysis of Random Waves and Loads - A Tutorial*. Math. Stat., Center for Math. Sci., Lund Univ., Lund, Sweden, 2000.

[51] G. Wei, J. T. Kirby, and A. Sinha. Generation of waves in Boussinesq models using a source function approach. *Coastal Eng.*, 36:271, 1999.

[52] T.-R. Wu. *A numerical study of three dimensional breaking waves and turbulence effects*. PhD thesis, Cornell University, 2004.

[53] Y. Yamazaki, Z. Kowalik, and K. F. Cheung. Depth-integrated, non-hydrostatic model for wave breaking and run-up. *Int. J. Numer. Meth. Fluids*, 61:473, 2009.

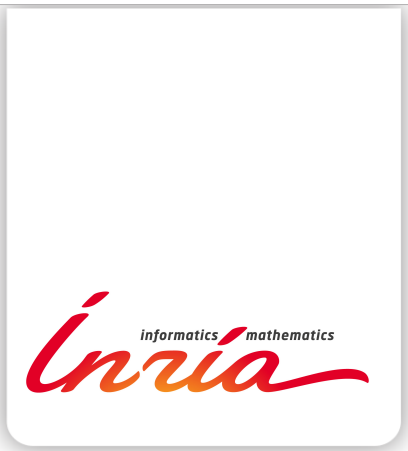

RESEARCH CENTRE
BORDEAUX – SUD-OUEST

200 avenue de la Vieille Tour
33405 Talence Cedex

Publisher
Inria
Domaine de Voluceau - Rocquencourt
BP 105 - 78153 Le Chesnay Cedex
inria.fr

ISSN 0249-6399